Open Archive Toulouse Archive Ouverte (OATAO)

Flame chemiluminescence from CO_2- and N_2-diluted laminar CH_4/air premixed flames

T.F. Guiberti [a,b,*], D. Durox [a], T. Schuller [a,c]

[a] *Laboratoire EM2C, CNRS, CentraleSupélec, Université Paris Saclay, Grande Voie des Vignes, 92290 Châtenay-Malabry, France*
[b] *King Abdullah University of Science and Technology (KAUST), Clean Combustion Research Center (CCRC), Thuwal, 23955-6900, Saudi Arabia*
[c] *Institut de Mécanique des Fluides de Toulouse (IMFT), Université de Toulouse, CNRS, INPT, UPS, Toulouse, France*

ABSTRACT

An experimental and numerical investigation of the chemiluminescence signals from OH^*, CH^*, and CO_2^* is conducted for laminar premixed conical CH_4/air flames diluted with CO_2 or N_2. Experiments are conducted either at fixed equivalence ratio or fixed adiabatic flame temperature. An ICCD camera, equipped with different narrow bandpass filters, is used to record flame images at 307 nm (OH^*), 430 nm (CH^*), and 455 nm (CO_2^*). A spectrometer is also used to correct the OH^* and CH^* emissions from the CO_2^* broadband background emission. Measured chemiluminescence intensities are then compared to one dimensional freely-propagating-flame direct simulations accounting for the chemistry of the excited radicals. Simulations predict accurately the OH^* chemiluminescence intensity, independently of the diluent nature and concentration. Correction for the CO_2^* background has a weak influence on the recorded OH^* signal. Predictions of CH^* emissions are also in good agreement with experimental data if the CO_2^* background intensity is subtracted from intensity measurements. Measured and calculated CO_2^* emissions lead to acceptable results using a simplified chemistry mechanism for CO_2^* and an heuristic model for its emission intensity. Finally, it is shown that CO_2 dilution modifies chemiluminescence intensity couples and particularly the OH^*/CO_2^* intensity ratio. These ratios regularly decrease with CO_2 dilution, a feature which is reproduced by the simulations. It is then shown that the ratio OH^*/CO_2^* is well suited to infer the CO_2 diluent concentration in diluted CH_4/air flames, a method which appears not feasible for sensing N_2 in N_2-diluted CH_4/air flames.

1. Introduction

In premixed hydrocarbon flames, the chemiluminescence from OH^* and CH^* excited radicals is generally intense. These emissions have thus been extensively used to infer properties of the reacting flow such as the heat release rate [1–9] or equivalence ratio [6,10–20], by examining the OH^*/CH^* intensity ratio. However, the OH^* and CH^* emission intensities need generally to be carefully corrected for the broadband CO_2^* background emission to achieve accurate measurements [6–8,18–22]. Additionally, most of the detailed chemistry mechanisms currently used in numerical simulations do not account for excited radicals chemistry due to the additional computational cost associated to the description of

their complex kinetics [12]. Simulations with simplified chemistry mechanisms are however often used to interpret chemiluminescence measurements with crude approximations on the relationship between non-excited species concentrations calculated by the solver and the excited radical species emission intensities that are measured. There is thus a gap between experiments and simulations with only a limited number of validations of the approximations made.

In this context, efforts are made to understand and model the complex chemistry of the formation and consumption of OH^* [24–28], CH^* [25–27,29–31], and CO_2^* [1,21,22,32] excited radicals. Comparisons between measurements and simulations in laminar [11,16,33] and turbulent [18–20,34] flames show that the detailed mechanisms developed for the chemistry of these excited radicals yield good results for lean and rich CH_4/air flames. In a recent work, García-Armingol and Ballester [19] analyzed numerically and experimentally the chemiluminescence of OH^*, CH^*, and CO_2^* in premixed turbulent swirling flames of $CH_4/CO_2/H_2/CO$/air blends. They emphasized the large differences in the emission

* Corresponding author at: King Abdullah University of Science and Technology (KAUST), Clean Combustion Research Center (CCRC), Thuwal, 23955-6900, Saudi Arabia.

E-mail addresses: thibault.guiberti@kaust.edu.sa, thibault.guiberti@gmail.com (T.F. Guiberti).

spectra from these flames in comparison to CH_4/air flames. They conducted 1-D Freely-Propagating-Flame (FPF) simulations as well as 0-D Perfectly-Stirred-Reactor (PSR) simulations to account for the change of turbulent combustion regime and examined effects of a large variety of mixtures and turbulent intensities. In this latter study, differences between measurements and simulations can be interpreted by either imprecisions in the selected detailed chemistry mechanisms or the inadequacy of the models used.

Another issue with turbulent flames is that the instantaneous flame surface area is generally not known. It is then difficult to compare, quantitatively, the measured chemiluminescence intensities to numerical results from 1-D FPF simulations, where the chemiluminescence intensities are computed per unit of flame surface area. This problem can however be circumvented by examining chemiluminescence intensity ratios between different couples of excited radicals. This method allows removing the contribution of the flame surface area [11,14,16,18–20]. In this case, species concentrations cannot however be compared directly.

For all these reasons, we decided to examine experimentally and numerically the chemiluminescence of OH^*, CH^*, and CO_2^* excited radicals in lean diluted methane/air premixed conical laminar flames, a configuration where the flame surface area is well defined. With proper care, conical laminar flames are readily comparable to adiabatic 1-D FPF direct simulations. Nori and Seitzman [35] studied effects of preheat temperature, pressure, and aerodynamic strain on the CH^* chemiluminescence to sense the equivalence ratio of methane and Jet-A flames burning in air. In the present study, focus is made on effects of CO_2 and N_2 dilutions in CH_4 fuel blends on the chemiluminescence of premixed flames.

CO_2 and N_2 diluted methane fuel blends are relevant for combustion applications powered by biogases, which are produced by methanization [36]. Biogases are classified as low heat value fuels and are mainly composed of CH_4, CO_2, and N_2 in variable proportions [37]. There is a growing interest for these renewable resources [38,39], which has led to applied research programs for adapting transport, heat, and power generation technologies to these new fuels [40–45].

Analysis of the chemiluminescence properties of CH_4/CO_2/N_2 fuel blends remain scarce. García-Armingol and Ballester [19] found that the increase in CO_2 content in CH_4/CO_2 mixtures reduces the intensity level of the emission spectra in the near UV and visible ranges, but it does not change the shape of these spectra. They attributed this effect to the weak influence of CO_2 on the chemistry of methane. Their simulations with an extended version of the GRI 3.0 detailed chemistry mechanism [46] reproduce well the evolution of the OH^*/CH^* ratio for mixtures with 25% and 50% (in volume) of CO_2 in CH_4/CO_2 blends. However, they did not consider emissions from CO_2^* and focused their work on sensing the equivalence ratio. Hossain and Nakamura [9] studied numerically the influence of N_2 and CO_2 dilution on CH^* chemiluminescence intensity in laminar counterflow diffusion flames. They reported a decrease of the CH^* intensity when increasing the diluent concentration, but numerical results were not compared to experiments. The OH^* and CO_2^* excited radicals were not examined in their study.

The present study has two main objectives. First, it is intended to determine the accuracy of a simplified chemistry mechanism yielding the OH^*, CH^*, and CO_2^* chemiluminescence intensities for CO_2- and N_2-diluted lean CH_4/air flames. The second objective is to examine the evolution of the OH^*, CH^*, and CO_2^* chemiluminescence intensities when CO_2 or N_2 diluent concentrations are varied in the fuel blend and investigate if the diluent concentration may be inferred from these data.

Methods including experimental setup, diagnostics, and numerical models are described in Section 2. Flame images are presented in Section 3.1 together with the way they are post-processed for
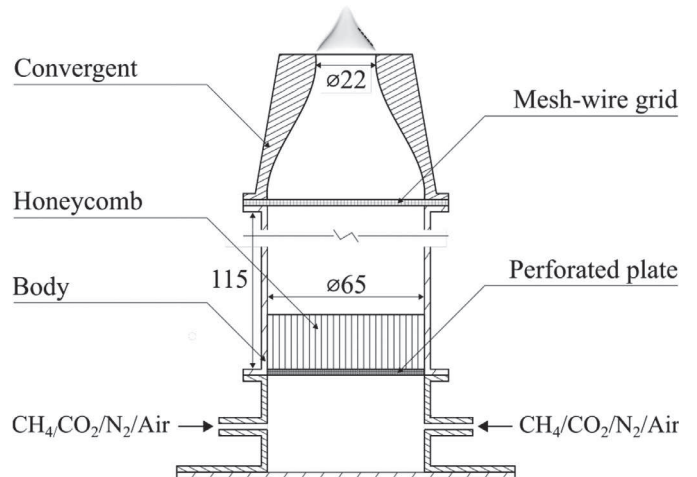

Fig. 1. Schematic of the burner with an example of flame image of a CH_4/air mixture injected at $\phi = 0.85$, $U = 57.9$ cm.s^{-1}, and $P = 600$ W.

the comparisons with numerical simulations. Results for experiments and simulations conducted at a fixed equivalence ratio are then presented. The influence of the CO_2^* background emission overlapping the OH^* and CH^* emission bands is characterized in Section 3.2. Effects of CO_2 and N_2 dilution on CO_2^* emissions are investigated in Section 3.3 and OH^* and CH^* emissions are examined in Section 3.4. These data are used to examine the evolution of intensity ratios in Section 3.5. All the analysis is finally briefly re-conducted for flames diluted at a fixed adiabatic flame temperature in Section 3.6.

2. Methods

2.1. Experimental setup

The experimental setup shown in Fig. 1 comprises an axisymmetric burner fed by mixtures of methane (CH_4), carbon dioxide (CO_2), and air. Alternatively, CO_2 can be replaced by nitrogen (N_2). The mixture enters the burner through a plenum and subsequently passes through a set of grid/honeycomb/grid before entering an injection nozzle with a cross-section contraction ratio of 8.7 and a 22 mm nozzle outlet diameter. This system yields a top hat velocity profile at the burner outlet with a reduced boundary layer thickness ($\sim$1 mm) that allows to stabilize laminar unconfined conical flames. The choice of a rather large exit diameter of 22 mm allows to minimize the influence of heat losses from the base of the flame to the burner rim and reduces effects of aerodynamic strain and flame curvature [47]. Conical flames with a nearly planar front over a large fraction of the flame surface can be stabilized. One example is shown in Fig. 1. Therefore, suitable conditions for comparisons with 1-D FPF direct simulations are reproduced.

The CO_2 dilution in the combustible mixture is expressed by the mole fraction of CO_2 in the CH_4/CO_2 blend and ranges here from $X_{CO_2}^{fuel} = 0$ to 0.40. When N_2 is used instead of CO_2 to dilute the flame, the diluent mixture fraction is varied between $0 \leq X_{N_2}^{fuel} \leq 0.55$. These values do not account for the N_2 naturally present in air. The mass flow rates of the different gases injected are regulated by thermal mass flow controllers (Bronkhorst, F-series). The mixture composition and bulk flow velocity U at the burner outlet are known with a relative accuracy better than 3%. Experiments are conducted at a fixed thermal power $P = 600$ W for gas injection at room temperature $T_0 = 300$ K and atmospheric pressure $p_0 = 1$ atm. In a first set of experiments, flames are diluted by

Table 1
Ranges of operating conditions explored for dilution at a fixed equivalence ratio $\phi = 0.85$ and thermal power $P = 600$ W, where U stands for the bulk flow velocity and T_{ad} for the adiabatic flame temperature.

$X_{diluent}^{fuel}$		0	0.05	0.10	0.15	0.20	0.25	0.30	0.35	0.40	0.45	0.50	0.55
N_2	T_{ad} (K)	2071	2065	2059	2052	2045	2036	2026	2015	2002	1987	1969	×
	U (cm.s^{-1})	57.9	58.1	58.4	58.7	59.1	59.5	59.9	60.4	61	61.7	62.6	×
CO_2	T_{ad} (K)	2071	2061	2051	2040	2027	2013	1997	1979	×	×	×	×
	U (cm.s^{-1})	57.9	58.1	58.4	58.7	59.1	59.5	59.9	60.4	×	×	×	×

Table 2
Ranges of operating conditions explored for dilution at a fixed adiabatic flame temperature $T_{ad} = 2071$ K and thermal power $P = 600$ W.

$X_{diluent}^{fuel}$		0	0.05	0.10	0.15	0.20	0.25	0.30	0.35	0.40	0.45	0.50	0.55
N_2	ϕ		0.850	0.854	0.859	0.864	0.870	0.876	0.884	0.893	0.904	0.918	0.935	0.957
	U (cm.s^{-1})		57.9	57.9	57.9	57.9	57.9	57.9	57.9	57.9	57.9	57.8	57.8	57.7
CO_2	ϕ		0.850	0.857	0.865	0.874	0.884	0.896	0.911	0.928	0.950	×	×	×
	U (cm.s^{-1})		57.9	57.7	57.5	57.3	57.0	56.7	56.4	56.0	55.4	×	×	×

keeping the equivalence ratio constant at $\phi = 0.85$ and increasing progressively the mole fraction of the diluent $X_{diluent}^{fuel}$ in the fuel mixture (Table 1). Another set of experiments is conducted by fixing the adiabatic flame temperature to $T_{ad} = 2071$ K and increasing $X_{diluent}^{fuel}$ (Table 2). In this case, the equivalence ratio ϕ is adjusted between the different cases explored. Therefore, the adiabatic flame temperatures T_{ad} [48] are first calculated for mixtures with both diluents, dilution ratios of the fuel blend $0 \leq X_{diluent}^{fuel} \leq 0.55$, and equivalence ratios $0.5 \leq \phi \leq 0.96$ to build a database. A lookup table is then used to match the equivalence ratio ϕ and operate the burner at the correct adiabatic flame temperature $T_{ad} = 2071$ K for all cases explored in Table 2. The cross symbols in Tables 1 and 2 designate conditions leading to blow-off.

2.2. Diagnostics

The flame chemiluminescence is investigated with two diagnostics. The first one is a 1024×1024-pixels ICCD camera (Princeton instruments, PI-Max 3) equipped with a UV lens (UV-NIKKOR, 105 mm, f/4.5) and different interferometric filters. A set of three 10 nm bandpass filters is used to collect the chemiluminescence signal from excited OH*, CH*, and CO_2* radicals, respectively centered at 307 nm (CVI, F10-307.1-4-50.0M), 430 nm (CVI, F10-430.0-4-50.0M), and 455 nm (Optoprim, 455BP10). Mean images are obtained by averaging 350 individual images, each with an exposure time of 3 ms. The total integration time is therefore 1.05 s. The signal-to-noise ratio (SNR) in these experiments is always higher than SNR = 26.

The second optical system is a low resolution inboard spectrometer (Ocean Optics, PC2000+UV–vis), coupled with a UV capable fiber optic, that records the broadband flame emission spectrum in the near-UV and visible ranges. The spectral resolution of this device, which is determined as the full width at half maximum (FWHM) of a He:Ne laser line at 632 nm, is 2.4 nm. Spectra presented in this study are not calibrated in relative intensities. Therefore, comparisons between OH*, CH*, and CO_2* absolute intensities are not possible. The exposure time is here set to 9 s and the spectrometer collects light over the whole flame region. The minimum SNR at 307 nm, 430 nm, and 455 nm are respectively $SNR_{307} = 25$, $SNR_{430} = 17$, and $SNR_{455} = 8$.

2.3. Numerical model

In addition to experiments, direct simulations of 1-D FPF are conducted with an internally developed solver [48] for the operating conditions shown in Tables 1 and 2. For this purpose, the detailed chemistry mechanism due to Lindstedt [49], without accounting for the NOx chemistry, is extended by including reactions

for the production and consumption of OH* [26] (9 reactions), CH* [26] (10 reactions), and CO_2* [22] (14 reactions) excited radicals. This extended mechanism includes 32 species and 174 reactions and can be found as supplementary electronic material. The sub-mechanism for OH* includes 1 production ($CH + O_2 \rightleftharpoons OH^* + CO$) and 8 consumption reactions, that are divided into 1 chemiluminescence and 7 quenching reactions. The reader is referred to [26] for more details. The excited radical CH* is produced via two main reactions [26]: $C_2H + O \rightleftharpoons CH^* + CO$ and $C_2H + O_2 \rightleftharpoons CH^* + CO_2$. Panoutsos et al. [16] made comparisons of simulations with the GRI 3.0 [46] and Lindstedt [49] chemistry mechanisms associated with a range of excited radical sub-mechanisms and found that the use of the Lindstedt mechanism coupled with the OH* and CH* mechanisms described in [26] yields the best results for lean CH_4/air flames. These mechanisms are selected here as well to investigate the chemiluminescence of OH* and CH* in diluted CH_4/air flames.

Two different models are used to simulate the chemistry of CO_2*. The first model, designated as detailed model in the following, includes 4 main production reactions [22]:

$$CO + O\,(+M) \rightleftharpoons CO_2^*\,(+M) \tag{1}$$

$$HCO + O \rightleftharpoons CO_2^* + H \tag{2}$$

$$H + H + CO_2 \rightleftharpoons CO_2^* + H_2 \tag{3}$$

$$CH_2 + O_2 + \rightleftharpoons CO_2^* + H + H \tag{4}$$

where M designates a third body partner. Kopp et al. [22] also introduced an additional CO_2* production reaction: $CH_3CHCO + OH \rightleftharpoons CO_2^* + C_2H_5$. This reaction cannot be included in our extended version of the Lindstedt mechanism because this mechanism does not account for CH_3CHCO. However, the sensitivity analysis presented in [22] shows that this reaction has only a weak influence in the predicted CO_2* mole fraction.

The second model designated here as simplified model uses a different method to simulate the CO_2* emission. Studies from Baulch et al. [32] and Kopp et al. [22] indicate that CO_2* is mainly produced through Eq. (1): $CO + O(+M) \rightleftharpoons CO_2^*(+M)$. Consequently, the CO_2* chemiluminescence intensity I_{CO_2} can be expressed as [21]:

$$I_{CO_2} = I_{CO_2}^0 [CO][O] \tag{5}$$

where [CO] and [O] stand for the concentrations of CO and O respectively and the rate $I_{CO_2}^0$ is a function of temperature, $I_{CO_2}^0 = 2.5 \times 10^6 \exp[-1600/T]$ [21]. A similar expression is used in [50],

Table 3
Reactions yielding the chemiluminescence of OH*, CH*, and CO₂*. The reaction rate is $k = AT^\beta \exp(-E/RT)$. Units are cal, cm, mole, s, and K. h stands for the Planck constant and ν corresponds to light frequency.

Chemiluminescence reaction		A	β	E
OH* [26]	OH* → OH + $h\nu$	1.45E+06	0	0
CH* [26]	CH* → CH + $h\nu$	1.85E+06	0	0
CO₂* [22]	CO₂* → CO₂ + $h\nu$	1.40E+06	0	0
CO₂* [21]	CO + O → CO₂ + $h\nu$	2.50E+06	0	3180

but the activation energy E and the pre-exponential factor A take different values to fit their measurements for atmospheric syngas/air and methane/air flames.

Table 3 summarizes the reactions yielding the chemiluminescence of OH*, CH*, and CO₂*. The light emission intensity is expressed here by the product of the Planck constant h and the emission frequency ν. Row 3 in this table corresponds to the detailed model for the calculation of CO₂* emission. Row 4 indicates how this emission is calculated with the simplified CO₂* model Eq. (5) without accounting for the detailed chemistry of CO₂*. This model reduces the cost of simulations. The three first rows in Table 3 indicate that the OH*, CH*, and CO₂* chemiluminescence intensities are directly proportional to the OH*, CH*, and CO₂* mole fractions. This is attributed to the fact that the corresponding reaction rates k do not depend on temperature ($\beta = E = 0$). The chemiluminescence intensity of these radicals is then calculated as the product of this excited radical mole fraction times the pre-exponential factor A.

3. Results and discussion

3.1. Analysis of flame images

It is worth starting the analysis by examining flame images obtained with the setup described in Section 2. Figure 2 shows mean images in false colors obtained with the ICCD camera equipped with the CVI F10-307.1-4-50.0M bandpass filter centered at 307 nm

for increasing concentrations of CO₂ in the fuel blend ranging from $X_{CO_2}^{fuel} = 0$ to 0.35. The equivalence ratio is kept constant to $\phi = 0.85$. Because experiments are carried out at a fixed thermal power $P = 600$ W, the injection bulk flow velocity increases from $U = 57.9$ cm·s⁻¹ at $X_{CO_2}^{fuel} = 0$ to $U = 60.4$ cm·s⁻¹ at $X_{CO_2}^{fuel} = 0.35$ (see Table 1). The flame length measured along the burner axis increases from $L = 19.3$ mm at $X_{CO_2}^{fuel} = 0$ to $L = 30.4$ mm at $X_{CO_2}^{fuel} = 0.35$. Images in this figure are all normalized by the maximum pixel value reached for the undiluted case shown on the left. The maximum OH* chemiluminescence intensity recorded thus decreases for increasing CO₂ concentrations. Experiments with N₂ as a diluent, not shown here, exhibit similar trends. Dilution with CO₂ or N₂ is known to alter flame chemistry [50,51] and laminar burning velocity S_L [47,52,53]. Flame lengthening is associated here to a decrease of the laminar burning velocity.

For each image in Fig. 2, the luminosity along the flame front remains roughly constant except close to the flame tip where it decreases abruptly. The region close to the tip appears less intense than the flame base. In this region, the flame has a high curvature leading to a modified balance between species and heat diffusion and a modified laminar burning velocity [54]. Here, however, the weaker luminosity is mainly attributed to small vertical oscillations of the flame tip position with time due to a buoyancy instability in the burnt gases that surround the flame [55,56]. The region at the flame tip appears thus artificially broadened in the long exposure time images and consequently features on average a lower local signal intensity. This effect limited to a narrow region over a small fraction of the flame surface area barely changes the global chemiluminescence signal intensity integrated over time and over the whole flame region.

Figure 3 shows CO₂-diluted flame images when the adiabatic flame temperature is kept constant at $T_{ad} = 2071$ K and the equivalence ratio is modified. Here again, the flame height increases with larger diluent concentrations and reaches $L = 19.3$ mm at $X_{CO_2}^{fuel} = 0$ and $L = 23.7$ mm at $X_{CO_2}^{fuel} = 0.35$. Dilution has however a weaker influence on the flame height than experiments conducted at a constant equivalence ratio shown in Fig. 2. This is attributed to the
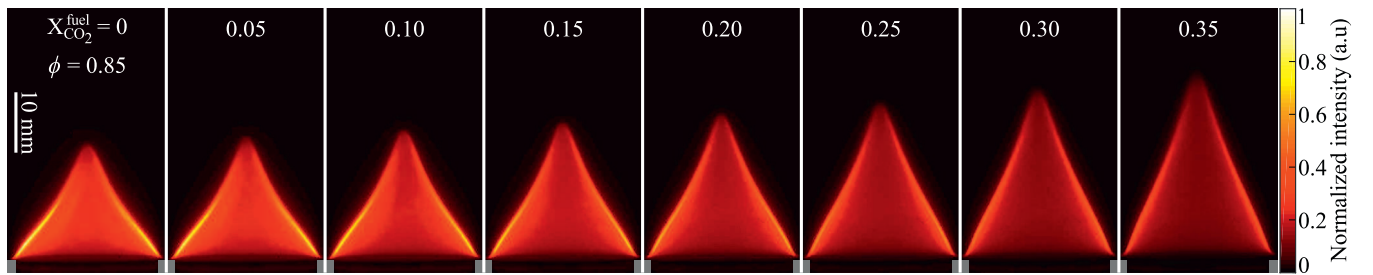

Fig. 2. Mean chemiluminescence images of CH₄/CO₂/air flames with $P = 600$ W, $\phi = 0.85$, and varying CO₂ mole fractions in the combustible mixture (see Table (1)). The ICCD camera is equipped with a 10 nm bandpass filter centered at 307 nm.
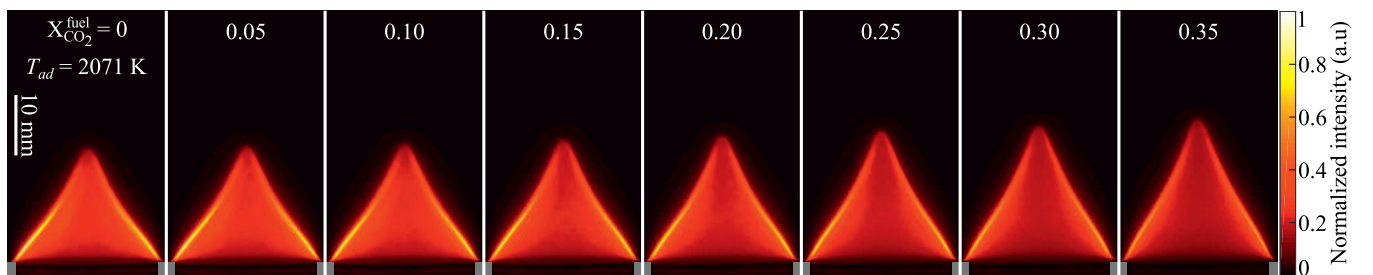

Fig. 3. Mean chemiluminescence images of CH₄/CO₂/air flames with $P = 600$ W, $T_{ad} = 2071$ K, and varying CO₂ mole fractions in the combustible mixture (see Table (2)). The ICCD camera is equipped with a 10 nm bandpass filter centered at 307 nm.
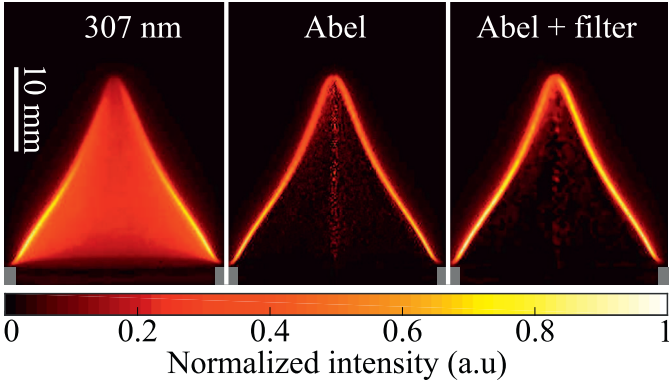
Fig. 4. Example of mean (left), Abel transformed (middle), and filtered (right) chemiluminescence images obtained with the bandpass filter centered at 307 nm for $P = 600$ W, $\phi = 0.85$, and $X_{CO_2}^{fuel} = 0.15$.
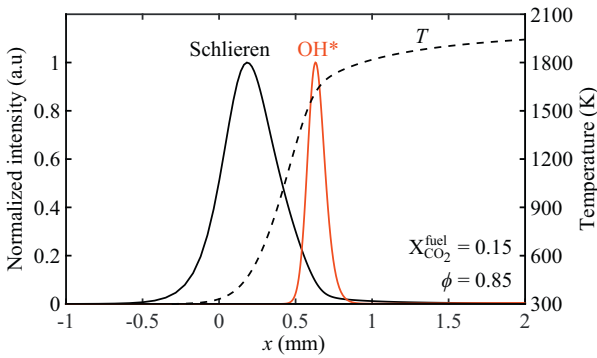

Fig. 5. Computed OH*, schlieren intensity ($(1/T^2)(\partial T/\partial x)$), and temperature T profiles for a flame at $P = 600$ W, $\phi = 0.85$, and $X_{CO_2}^{fuel} = 0.15$.

Fig. 6. Measured flame surface area for CH_4/air flames diluted with CO_2 (top) or N_2 (bottom). Results are presented for dilutions at a fixed equivalence ratio $\phi = 0.85$ (black) or adiabatic flame temperature $T_{ad} = 2071$ K (red). The flame front tracer is the maximum OH* chemiluminescence intensity (square symbols) or the simulated maximum schlieren intensity (circle symbols). (For interpretation of the references to color in this figure legend, the reader is referred to the web version of this article.)

increase of equivalence ratio (see Table 2) that enhances the laminar burning velocity S_L and compensates effects of dilution to a certain extent. The same remark can be made for the OH* chemiluminescence intensity. The OH* reduction observed in Fig. 3 when the diluent concentration increases is weaker than in Fig. 2. Results for chemiluminescence intensities are compared on a more quantitative basis in the following sections.

To allow comparisons with 1-D direct simulations, experimental data need to be rescaled by the flame surface area, which can be obtained by post-processing the mean chemiluminescence images presented in Figs. 2 and 3. For each operating condition investigated, an Abel transformation is first applied on the raw images recorded by the ICCD camera equipped with the CVI F10-307.1-4-50.0M bandpass filter to determine the OH* chemiluminescence signal originating from a central vertical plane passing through the burner axis (Fig. 4 left and middle). A 10×10-pixels median filter is then applied on the resulting images to reduce the noise produced by the Abel transformation (Fig. 4 right). A homemade Matlab® routine then computes the flame surface area from the filtered images. In this study, the OH* signal is used to delineate the flame front position, which is identified as the position of maximum OH* chemiluminescence intensity. The OH* signal takes its highest values in the hottest regions of the flame and is offset with respect to the beginning of the preheated region usually used to define the flame surface area [16]. For laminar burning velocity measurements, the schlieren or shadowgraphy techniques are therefore often preferred to infer precisely the flame front position [47,52,57]. Figure 5 shows the computed normalized OH* chemiluminescence intensity and the temperature profile for a flame at $P = 600$ W, $\phi = 0.85$, and $X_{CO_2}^{fuel} = 0.15$ calculated with the code de-

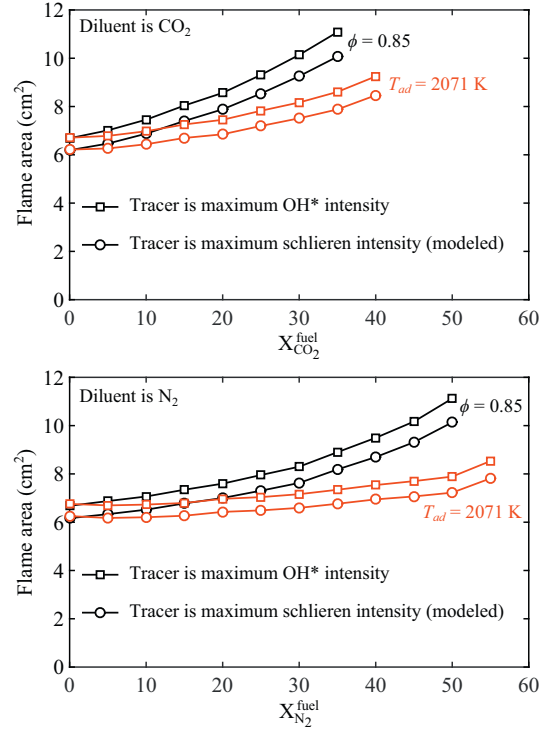scribed in Section 2.3. A synthetic schlieren signal profile, defined as $(1/T^2)(\partial T/\partial x)$ [58] with T and x being the temperature and the progress along a coordinate normal to the flame front, is also plotted. The origin $x = 0$ in this figure corresponds to the beginning of the preheat zone. The maximum schlieren intensity lies at a position $x = 0.18$ mm located 0.45 mm upstream the OH* peak intensity detected at $x = 0.63$ mm. Simulations show that the distance between the schlieren and OH* peaks is always comprised between 0.41 mm and 0.54 mm for the operating conditions investigated in Tables 1 and 2.

Figure 6 shows the measured flame surface area (square symbols) deduced from the OH* signals as a function of the diluent concentration with CO_2 (top) or N_2 (bottom) for experiments conducted at a fixed equivalence ratio (black) and at a fixed adiabatic flame temperature (red). Knowing the distance $d = 0.48 \pm 0.6$ mm between the OH* peak intensity and schlieren front allows to plot a corrected flame surface area (circle symbols) that would be measured by a schlieren technique. Comparison between these two quantities shows that calculations with the OH* tracer overestimates the flame surface area by about $9 \pm 1\%$ on average compared to that deduced with a synthetic schlieren signal. This difference remains roughly constant and corresponds to a constant offset for all cases explored. In what follows, all chemiluminescence intensities are normalized by the peak value obtained for the undiluted reference case $X_{diluent}^{fuel} = 0$ at $\phi = 0.85$. Due to the roughly constant offset between the flame surface areas deduced from the OH* and the synthetic schlieren signals, the OH* signal can, in this study, safely be used to determine the flame surface areas needed to normalize the chemiluminescence data. This procedure is applied to compare results from 1-D FPF simulations with experiments.
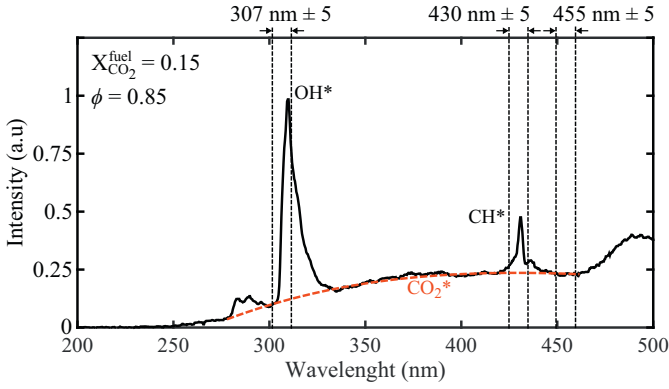
Fig. 7. Flame spontaneous emission spectrum for $P = 600$ W, $\phi = 0.85$, and $X_{CO_2}^{fuel} = 0.15$. Vertical dashed lines show the width of the bandpass filters used during the ICCD experiments.
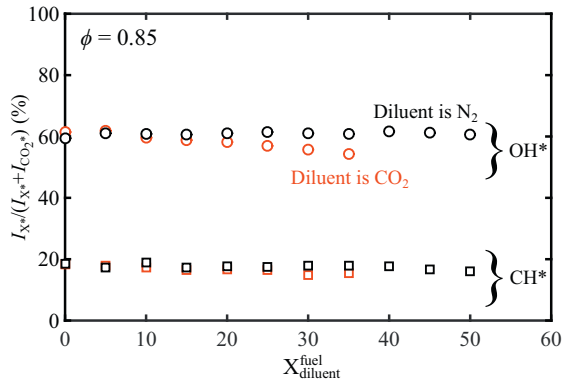
Fig. 8. Chemiluminescence intensities emitted by OH* (circle symbols) within [278–336 nm] and CH* (square symbols) within [416–449 nm] and normalized by the total chemiluminescence intensity emitted by both OH* and CO_2* or CH* and CO_2*, respectively. Results are presented as a function of the mole fraction of diluent, N_2 (black) or CO_2 (red), in the fuel for $\phi = 0.85$. (For interpretation of the references to color in this figure legend, the reader is referred to the web version of this article.)

3.2. Effects of CO_2* emission background

We now aim at determining effects of CO_2* on flame emission spectra between 200 and 500 nm. Figure 7 shows a spontaneous emission spectrum for a CH_4/CO_2/air flame at $\phi = 0.85$ and $X_{CO_2}^{fuel} = 0.15$. The spectrum exhibits two narrow peaks around 309 nm and 432 nm that are characteristics of OH* and CH* chemiluminescence emissions [14]. One also identifies the broadband continuous light emission from CO_2* [21], that has been fitted here by the red dashed line between 270 and 460 nm. Figure 7 shows that placing the CVI F10-307.1-4-50.0M narrow bandpass filter centered at 307 nm in front of the ICCD camera does not allow to only select the OH* emission because the CO_2* background emission has already a sizable contribution at these wavelengths. This problem was already reported in [7,8,18,19]. The same phenomenon is observed at 430 nm for the CH* excited radical with a larger contribution from the CO_2* background emission intensity to the light recorded by the spectrometer. Figure 7 also shows that a bandpass filter centered at 455 nm allows to select only the chemiluminescence from excited CO_2* radicals.

It is worth examining the contribution of the CO_2* intensity background to OH* and CH* chemiluminescence intensities in more details. Figure 8 plots the OH* intensity, I_{OH*}, recorded in the range [278–336 nm]. This wide spectral width takes most of the OH* emission bands into account as shown in Fig. 7. Results

in Fig. 8 are normalized by the total chemiluminescence intensity emitted by both OH* and CO_2* excited radicals, $I_{OH*} + I_{CO_2^*}$, over the same spectral range. Results are presented as a function of the diluent mole fraction in the fuel for $\phi = 0.85$. The OH* intensity I_{OH*} is computed as follows:

$$I_{OH*} = \int_{278}^{336} [S(\lambda) - B(\lambda)]\, d\lambda \tag{6}$$

where λ is the wavelength, S stands for the spectrometer measured intensity (black solid line), and B represents the fitted CO_2* chemiluminescence intensity (red dashed line) $I_{CO_2^*}$:

$$I_{CO_2^*} = \int_{278}^{336} B(\lambda)\, d\lambda \tag{7}$$

For N_2-diluted flames, Fig. 8 shows that the OH* chemiluminescence intensity corresponds roughly to 60% of the total chemiluminescence intensity detected in the spectral range [278–336 nm] that includes both the OH* and CO_2* contributions. Increasing N_2 dilution has only a weak influence on the fraction of light emitted by OH*, but the CO_2* background intensity cannot be neglected. For CO_2-diluted flames, the contribution of the CO_2* background intensity increases with the CO_2 concentration and leads to a drop of I_{OH*} with respect to $I_{OH*} + I_{CO_2*}$ in Fig. 8. The ratio $I_{CO_2*}/(I_{OH*} + I_{CO_2*})$ reaches 46% at $X_{CO_2}^{fuel} = 0.35$. For large CO_2 dilution concentrations $X_{CO_2}^{fuel} > 0.40$, which could not be explored in these experiments due to blow-off issues, the CO_2* chemiluminescence intensity might exceed the OH* chemiluminescence intensity over the range [278–336 nm]. These conditions would correspond to a weak OH* emission peak around 307 nm flooded within a continuous CO_2* background emission. In this case, narrow bandpass filters (FWHM < 10 nm) centered around the wavelength of maximum OH* emission must be preferred. To illustrate it, the chemiluminescence intensity recorded with the CVI F10-307.1-4-50.0M bandpass filter allows to collect more than 77% of the light intensity originating from OH* radicals even at large CO_2 concentrations $X_{CO_2}^{fuel} = 0.35$. This large value also proves that it is not necessary to correct the OH* images collected with the F10-307.1-4-50.0M filter that are used to determine the flame surface area. It should also be noted that the values plotted in Fig. 8 cannot be used to correct OH* images because the range of wavelengths used for computations does not match the transmission band of the F10-307.1-4-50.0M filter.

The same analysis is now carried in Fig. 8 for the CH* spontaneous emission band around 430 nm integrated over a 33 nm spectral bandwidth. The CH* chemiluminescence intensity I_{CH*}, detectable in the range [416–449 nm], is computed as follows:

$$I_{CH*} = \int_{416}^{449} [S(\lambda) - B(\lambda)]\, d\lambda \tag{8}$$

where $I_{CO_2^*}$ is now:

$$I_{CO_2^*} = \int_{416}^{449} B(\lambda)\, d\lambda \tag{9}$$

Independently of the diluent nature and its concentration in the mixture, around 80% of the signal intensity detected in the spectral range [416–449 nm] originates from CO_2* and not from CH*. A narrow bandpass filter centered around the CH* maximum emission peak near 430 nm, like the CVI F10-430.0-4-50.0M filter with a FWHM $\simeq 10$ nm used in this study, allows to reduce the contribution of CO_2* intensity to less than 65%. In any cases, it is necessary to correct for the CO_2* intensity background if the CH* intensity needs to be analyzed precisely. This is illustrated in Fig. 9.

Figure 9 left shows an Abel inverted image of the light recorded with the ICCD camera equipped with the CVI F10-430.0-4-50.0M bandpass filter centered at 430 nm for a CO_2-diluted flame at
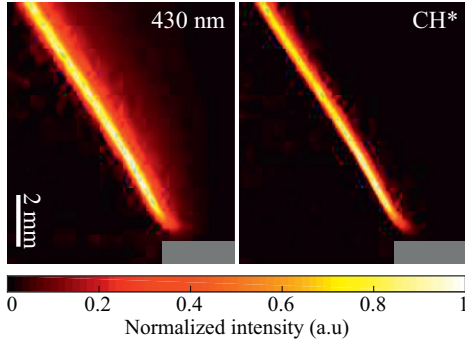
Fig. 9. Left: Abel transformed image of the light detected by the ICCD camera equipped with the CVI F10-430.0-4-50.0M bandpass filter centered at 430 nm for a flame at $P = 600$ W, $\phi = 0.85$, and $X_{CO_2}^{fuel} = 0.15$. Only the region near the flame base is presented. Right: Post-processed image obtained after subtraction of the CO_2^* intensity background.

$P = 600$ W, $\phi = 0.85$, and $X_{CO_2}^{fuel} = 0.15$. Only the region close to the flame base is shown in this figure. This image features a relatively broad region with high pixel values revealing light emission over a region extending over more than 1 mm. This is attributed to the emission of CO_2^* because the CH* radical cannot be present so far downstream in the burnt gases for these operating conditions [11,16,33,34]. The same setup was used but with the ICCD camera equipped with the Optoprim 455BP10 bandpass filter centered at 455 nm, *i.e.* close to the CH* emission range, to record only the CO_2^* emission intensity. This image is then used to remove the CO_2^* contribution from the image shown in Fig. 9 left [7,8]. This is suitable because the CO_2^* emission spectrum remains roughly flat in the range [420–460 nm] (Fig. 7). The result of this correction is presented in Fig. 9 right. This new image shows a narrow region with high pixel values well delineating the reaction layer and there is no significant signal few tens of millimeters downstream the reaction zone. The signal shown in this image can now be attributed to the CH* emission only.

3.3. Effects of CO_2 and N_2 dilution on CO_2^*

Focus is now made on the influence of CO_2 and N_2 dilution on the chemiluminescence of CO_2^*. The flame surface areas plotted in Fig. 6 are used to normalize the chemiluminescence intensities measured with the ICCD camera equipped with the Optoprim 455BP10 bandpass filter centered at 455 nm. The CO_2^* signal measured by the spectrometer over the same spectral bandwidth as

the Optoprim 455BP10 filter is also corrected by the flame surface area to yield $I_{CO_2^*} = \int_{450}^{460} S(\lambda) d\lambda$.

It is first worth examining the evolution of the light intensity in the normal direction to the flame front. Figure 10 shows the normalized profiles of the measured CO_2^* chemiluminescence intensity (black solid line) as a function of the distance x to the flame front for CO_2-diluted flames at $P = 600$ W and $\phi = 0.85$. Results are presented for different diluent concentrations $X_{CO_2}^{fuel} = 0$, 0.25, and 0.35. The location of the maximum CO_2^* peak intensity is used here to define the origin of the normal axis $x = 0$. Negative values $x < 0$ correspond to the reactant side. These profiles are probed at a height of 4 mm above the burner lip to minimize both the influence of heat losses to the burner and oscillations of the flame tip position. Starting from the fresh reactants ($x < 0$), one can notice a very sharp increase of the CO_2^* chemiluminescence intensity near $x \simeq 0$. The CO_2^* chemiluminescence intensity then slowly decreases in the post-flame region ($x > 0$) and vanishes for $x > 3$ mm for all diluent concentrations explored. Away from the flame tip and flame base, these features are found to be independent of the height above which the experimental profiles are sampled.

The blue dashed lines in Fig. 10 show results for the normalized CO_2^* intensity profiles calculated with the simplified CO_2^* chemiluminescence model based on O and CO mole fractions (Table 3, row 4). The location of the CO_2^* peak intensity is used to rescale simulations with experiments at $x = 0$. The measured and the calculated CO_2^* profiles match well for the three dilutions explored. This simplified CO_2^* chemiluminescence model is able to accurately reproduce the rate of consumption of CO_2^* in the post-flame region due to both chemiluminescence and quenching reactions. The red dashed lines in Fig. 10 show the computed normalized CO_2^* chemiluminescence intensity profiles calculated with the detailed chemistry mechanism (Table 3, row 3). This model largely overestimates the consumption rate of CO_2^* in the post flame region and consequently fails to capture the CO_2^* chemiluminescence intensity in this region. This remains true over the whole range of dilution ratios examined. At this stage, there is no interpretation for the behavior of the detailed mechanism that fails to capture the CO_2^* emission in the burnt gases. The simplified model based on O and CO mole fractions (Table 3, row 4) yields better predictions of CO_2^* relative concentrations.

Signals integrated over the whole flame region and normalized by the flame surface area are now examined. Figure 11 top plots the measured CO_2^* chemiluminescence intensity as a function of the CO_2 mole fraction in the fuel when the equivalence ratio is kept constant and equal to $\phi = 0.85$. Results are normalized by the value obtained for the undiluted flame when $X_{CO_2}^{fuel} = 0$. Hollow
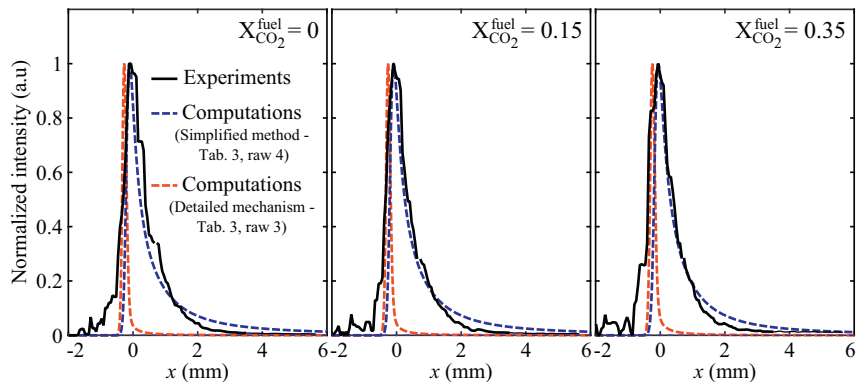
Fig. 10. Normalized profiles of the measured (black solid line) and computed (blue and red dashed lines) CO_2^* chemiluminescence intensity as a function of the distance to the flame front x for flames at $P = 600$ W and $\phi = 0.85$. Negative and positive values of x correspond to the reactant and burnt gases sides, respectively. Results are presented for three flames featuring different dilution ratios $X_{CO_2}^{fuel} = 0$ (left), 0.15 (middle), and 0.35 (right). (For interpretation of the references to color in this figure legend, the reader is referred to the web version of this article.)
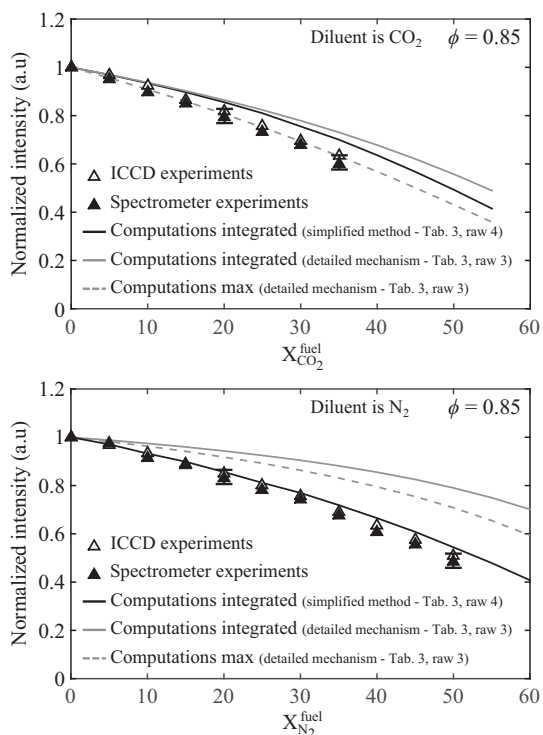
Fig. 11. Measured (symbols) and computed (lines) of CO_2^* chemiluminescence intensity as a function of the diluent mole fraction in the combustible mixture. Diluent is CO_2 (top) or N_2 (bottom).

triangle symbols stand for the chemiluminescence intensity measured by the ICCD camera equipped with the 10 nm Optoprim 455BP10 bandpass filter centered at 455 nm and averaged over the whole flame region. These data are compared with the CO_2^* emission intensities recorded by the spectrometer (black triangle symbols) and integrated over the spectral range [450–460 nm]. Experiments with the ICCD camera and the spectrometer yield results that collapse on the same curve up to $X_{CO_2}^{fuel} = 0.35$. It was also checked that the CO_2^* chemiluminescence intensities calculated with the spectrometer data integrated over different spectral ranges produce similar results (see supplementary electronic material). The spectral distribution of the broadband CO_2^* chemiluminescence intensity remains unchanged within the range of operating conditions covered in Tables 1 and 2.

In Fig. 11 and the consecutive figures, error bars are presented for the chemiluminescence intensities recorded with the spectrometer and corrected for the broadband CO_2^* background emission (filled symbols). Values for the chemiluminescence intensities are obtained through the post-processing steps described in Sections 3.1 and 3.2 and are therefore sensitive to a number of input parameters such as the order of the polynomial for the fitted CO_2^* background intensity, the size of the median filter for the determination of the flame surface area, and the wavelength range chosen for integration of the emission spectra. The magnitude of error bars is therefore determined by assessing the sensitivity of the chemiluminescence intensity to these various input parameters whose most appropriate values are, a priori, not known. Through the paper, variations of measured OH^*, CH^*, and CO_2^* chemiluminescence intensities as a function of the diluent concentration and diluent nature are considered meaningful if they exceed experimental uncertainties, represented by these error bars.

Figure 11 top shows that dilution with CO_2 leads to a smooth decrease of the measured CO_2^* intensity. This signal drops by 40% when the mole fraction of CO_2 in the fuel reaches $X_{CO_2}^{fuel} = 0.35$.

Figure 11 bottom shows that experiments made with the ICCD camera and the spectrometer for N_2-diluted CH_4/air flames again lead to the same results up to $X_{N_2}^{fuel} = 0.50$. The CO_2^* emission intensity also decreases for increasing N_2 concentrations in the fuel blend. For the same equivalence ratio $\phi = 0.85$, the CO_2^* intensity decays more slowly for N_2-diluted fuel blends than with CO_2 dilution. The CO_2^* intensity drops by 40% drop for $X_{N_2}^{fuel} = 0.45$ approximately.

The evolution of the CO_2^* intensity, integrated in the normal direction and rescaled for a 1 m^2 flame surface area, calculated by the numerical solver and the CO_2^* detailed mechanism (Table 3, row 3) is plotted in Fig. 11 top as a function of the CO_2 diluent mole fraction (gray solid line). These simulations also reproduce the decay of the CO_2^* chemiluminescence intensity as dilution increases. However, they underestimate the rate of decay of the CO_2^* chemiluminescence intensity by approximately 30%. Another attempt was made by plotting as dashed gray lines the evolution of the calculated peak CO_2^* intensity reached in each flame. Agreement between experiments and simulations slightly improves for the CO_2-diluted flames investigated. Results with the simplified CO_2^* model synthesized in Table 3, row 4 are plotted as the solid black curve in Fig. 11 top when the numerical signal is integrated along the normal to the flame front. Agreement between experiments and simulations is acceptable, with relative differences limited to 7%. Results with the simplified CO_2^* model are in better agreement with measurements than those found with the detailed mechanism for CO_2^*. Calculations of CO_2^* chemiluminescence intensities using the values for the activation energy E and the pre-exponential factor A from [50] were also carried out and they yield similar results. They are not reproduced here.

When CO_2 is replaced by N_2, Fig. 11 bottom shows that the simplified CO_2^* model yields an accurate prediction of the measured evolution of the CO_2^* chemiluminescence intensity, while the detailed model for CO_2^* fails to predict accurately the drop of CO_2^*, independently of the way calculations are post-processed. These tests confirm that the CO_2^* intensity can be simulated adequately for N_2- and CO_2-diluted CH_4 fuel blends provided that the simplified CO_2^* in Table 3 row 4 is used. All the simulations are thus conducted with this model in the remaining parts of this study.

3.4. Effects of CO_2 and N_2 dilution on OH^* and CH^*

Effects of dilution on the OH^* and CH^* emissions are now examined. Results for the CO_2^* excited radical are repeated for comparison purposes. Figure 12 top shows the measured CO_2^* (black triangles), OH^* (blue circles), and CH^* (red squares) intensities as a function of the CO_2 mole fraction in the fuel for lean flames at a fixed equivalence ratio $\phi = 0.85$. Results are again normalized by the value obtained for the undiluted flame. Hollow and solid symbols stand for the chemiluminescence intensities measured with the ICCD camera and the spectrometer, respectively. The OH^* and CH^* intensity levels measured with the ICCD camera are not corrected for the CO_2^* intensity background in this figure. However, the intensities deduced from spectrometer measurements are corrected for the CO_2^* intensity background. This figure shows that the emission intensity from these three excited radicals regularly decreases when the CO_2 concentration in the fuel increases. The OH^* chemiluminescence intensity drops by 57% when $X_{CO_2}^{fuel} = 0.35$. It is known that increasing the CO_2 concentration in the combustible mixture reduces the concentration of CH in the flames [59]. The production of OH^* is then penalized because this excited radical is mainly produced through the formation reaction: $CH + O_2 \rightleftharpoons OH^* + CO$ [16,23]. Results for OH^* obtained by subtracting the CO_2^* background (blue disks) are on average only 4% lower than the measured OH^* intensities without correction (blue circles)
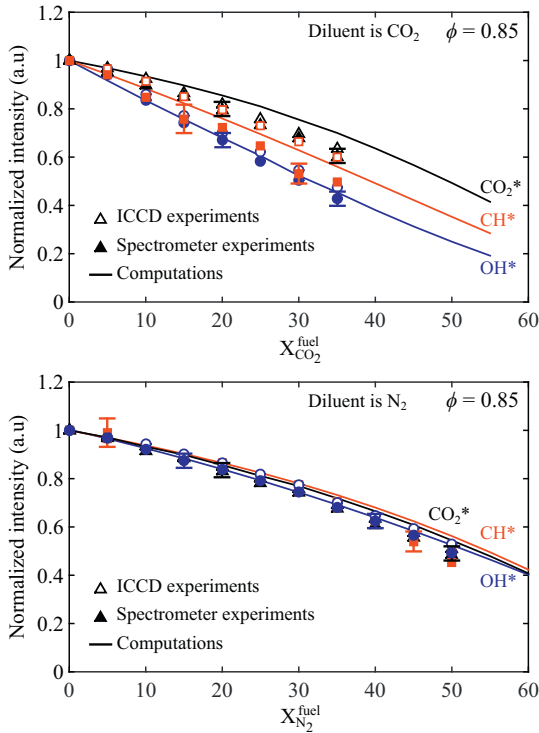
Fig. 12. Measured (symbols) and computed (lines) normalized spontaneous emission intensities of OH* (blue), CH* (red), and CO_2* (black) as a function of the diluent mole fraction in the combustible mixture. Hollow and solid symbols stand for ICCD camera and spectrometer measurements, respectively. Experiments are realized at a fixed equivalence ratio $\phi = 0.85$. Diluent is CO_2 (top) or N_2 (bottom). (For interpretation of the references to color in this figure legend, the reader is referred to the web version of this article.)

in Fig. 12 top. As already indicated in the previous section, correction for the CO_2* background intensity has only a weak influence in the spectral bandwidth of OH* spontaneous emission.

Conversely, correction for the CO_2* background has a large influence on the measured CH* emission levels, as shown in Fig. 12 top where data deduced from the spectrometer (filled red squares) lie below those obtained with the ICCD camera (red squares) equipped with the CVI F10-430.0-4-50.0M bandpass filter centered at 430 nm. This is in agreement with results presented in Fig. 8 where the majority of the signal detected by the ICCD camera around 430 nm comes from CO_2* emission. Removing the CO_2* background intensity reduces the measured CH* emission level by 10% on average. It is however worth noting that the subtraction of the CO_2* background intensity leads to larger error bars for the deduced CH* intensity levels in Fig. 12 top.

Data for lean N_2-diluted flames at $\phi = 0.85$ are presented in Fig. 12 bottom. The OH*, CH*, and CO_2* measured intensities collapse here on the same curve. The intensity of these excited radicals regularly decreases for increasing N_2 mole fractions in the fuel. A similar effect of N_2 dilution was reported in [9] for the CH* chemiluminescence intensity. The OH*, CH*, and CO_2* emission levels drop by approximately 30% and 50% when $X_{N_2}^{fuel} = 0.35$ and $X_{N_2}^{fuel} = 0.50$, respectively. For the same mole fraction in the fuel mixture, dilution with N_2 has a smaller effect on the OH* and CH* chemiluminescence intensities than dilution with CO_2.

The black, blue, and red solid lines in Fig. 12 show the computed intensities from CO_2*, OH*, and CH*, respectively. The CO_2* chemiluminescence intensity plotted here is calculated with the simplified model described in Table 3, row 4. Simulations reproduce well experiments for the OH* signal for both CO_2- and

N_2-diluted mixtures. Measurements corrected for the CO_2* background emission intensity however only barely reduce relative differences that are limited to 3%.

In the case of CO_2-diluted flames, differences between measurements and predictions are more important in Fig. 12 (top) for the CH* emission intensity, with a mean difference of 7%. However, this difference barely exceeds experimental uncertainties. Simulations yield a better match with CH* experimental data that are not corrected for the CO_2* background emission. This may be due to the relatively low ratio between the CH* signal and the CO_2* background intensity leading to large uncertainties in the corrected CH* chemiluminescence intensities (see Figs. 7 and 8). For N_2-diluted flames shown in Fig. 12 bottom, simulations reproduce well measurements for the three radicals and over the whole range of dilution explored. The mean relative difference between measurements and simulations only reaches 2%, 5%, and 6% for OH*, CO_2*, and CH*, respectively.

For most of the operating conditions, the detailed chemistry mechanisms for OH* and CH*, as well as the simplified model to compute the CO_2* intensity, yield good results. It is also worth noting that the subtraction of the CO_2* background intensity has only a weak influence on the integrated results shown in Fig. 12. This is attributed to the comparable influence of dilution on the three excited radicals emission intensities. Their intensity decreases at about the same proportion when the diluent concentration increases, especially for N_2-diluted flames.

3.5. Analysis of OH*, CH*, and CO_2* intensity ratios

In many applications, the flame surface area is not known and is difficult to measure. This is the case for turbulent flames where the reaction layer has a 3-D structure and fluctuates with time. In such cases, it is difficult to normalize the measured chemiluminescence intensities by the flame surface area. Comparison between measured intensities and 1-D simulations is then more difficult. Consequently, chemiluminescence intensity ratios between different couples of excited radicals are often examined because they allow to remove the contribution of the flame surface area [11,14,16,18–20]. Effects of CO_2 and N_2 dilutions on these ratios are examined here.

Figure 13 shows the measured OH*/CH* (black circle), OH*/CO_2* (red squares), and CH*/CO_2* (blue triangles) intensity ratios as a function of the diluent mole fraction in the fuel, after the contribution of the CO_2* background has been removed using the spectrometer experiments. Results are presented for CO_2-diluted (top) and N_2-diluted (bottom) flames and are normalized by the value obtained for the undiluted case. The experimental data feature larger error bars than in the previous figures due to the cumulative relative errors on the numerator and denominator of the intensity ratios. Error bars are only plotted in this figure for three operating conditions to illustrate the confidence range.

When dilution is made with CO_2 (Fig. 13 top), these three intensity ratios decrease when the mole fraction of CO_2 in the fuel increases. For example, the measured OH*/CO_2* intensity ratio drops by nearly 30% for $X_{CO_2}^{fuel} = 0.35$. The decay rate of two other intensity couples OH*/CH* and CH*/CO_2* with CO_2 dilution is the same and takes a lower value than for the OH*/CO_2* couple. When dilution is made with N_2 (Fig. 13 bottom), these chemiluminescence intensity ratios remain roughly constant within the confidence interval when the diluent concentration is increased. All of these features are also well captured by the simulations both for N_2- and CO_2-diluted flames, except for large N_2 concentrations $X_{N_2}^{fuel} > 0.40$.

These results indicate that after careful calibration, monitoring the OH*/CO_2* chemiluminescence intensity ratio may allow inferring the CO_2 diluent concentration in lean CH_4/CO_2/air flames.
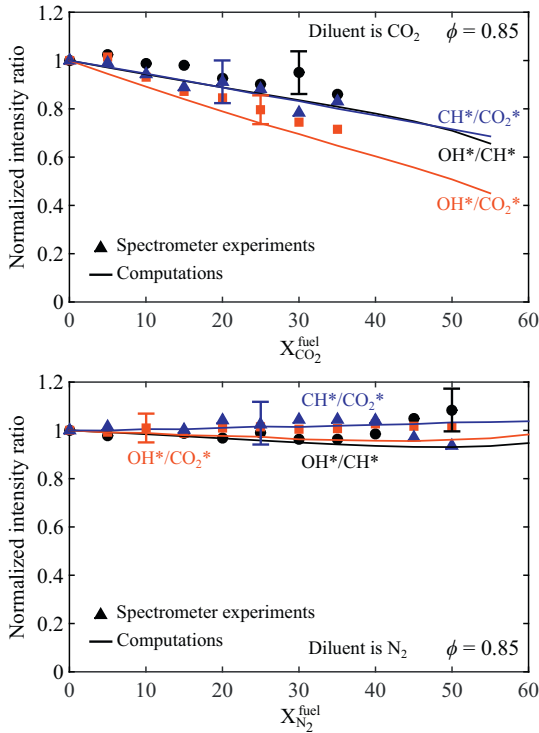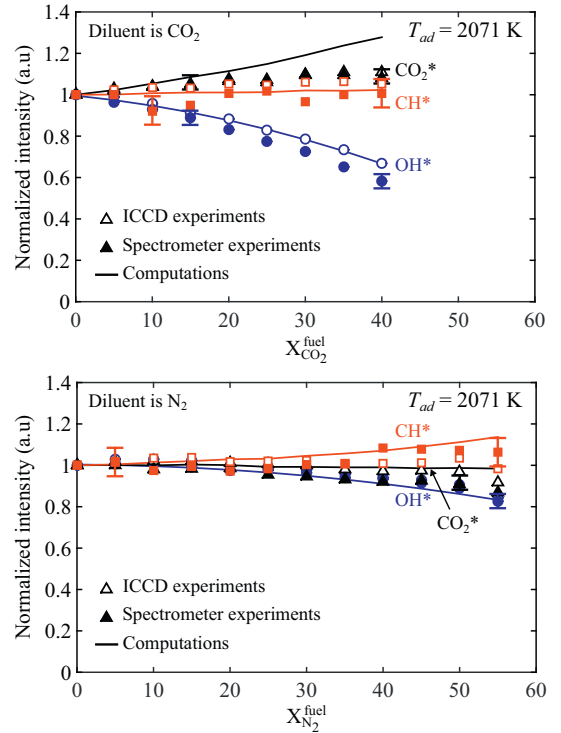
Fig. 13. Measured (symbols) and computed (lines) normalized OH*/CH* (black), OH*/CO₂* (red), and CH*/CO₂* (blue) intensity ratios as a function of the diluent mole fraction in the combustible mixture for CH_4/air/diluent mixtures at a fixed equivalence ratio $\phi = 0.85$. Diluent is CO_2 (top) or N_2 (bottom). (For interpretation of the references to color in this figure legend, the reader is referred to the web version of this article.)

Fig. 14. Measured (symbols) and computed (lines) normalized chemiluminescence intensities of OH* (blue), CH* (red), and CO₂* (black) radicals as a function of the diluent mole fraction in the fuel when dilution is realized at a fixed adiabatic flame temperature $T_{ad} = 2071$ K. Hollow and solid symbols stand for ICCD camera and spectrometer measurements, respectively. Diluent is CO_2 (top) or N_2 (bottom). (For interpretation of the references to color in this figure legend, the reader is referred to the web version of this article.)

However, this technique cannot be used for N_2-diluted CH_4/air flames.

3.6. Analysis of dilution effects at a fixed adiabatic flame temperature

So far the chemiluminescence data for CH_4 fuel blends diluted with N_2 or CO_2 was examined at a fixed equivalence ratio $\phi = 0.85$. The influence of dilution on the chemiluminescence intensities for mixtures diluted at a fixed adiabatic flame temperature $T_{ad} = 2071$ K (see Table 2) is now examined. Figure 14 top plots the measured CO_2* (black triangles), OH* (blue circles), and CH* (red squares) chemiluminescence intensities as a function of the CO_2 mole fraction in the fuel blend. Results are normalized by the value obtained for the undiluted flame. Hollow and solid symbols stand for the chemiluminescence intensities measured by the ICCD camera and the spectrometer, respectively.

Here again, the OH* chemiluminescence intensity decreases regularly with the CO_2 dilution ratio. The OH* intensity drops by approximately 40% at $X_{CO_2}^{fuel} = 0.40$. The CH* emission intensity remains roughly constant even for large CO_2 concentrations while the CO_2* chemiluminescence intensity slightly increases with dilution. For example, the CO_2* intensity increases by approximately 10% at $X_{CO_2}^{fuel} = 0.40$ with respect to the signal measured for the undiluted flame. This weak effect of dilution on the CH* intensity is due to the increase of the equivalence ratio [16] needed to obtain a diluted mixture featuring the same adiabatic flame temperature as a less diluted one. This slight increase of the equivalence ratio compensates the influence of dilution (see Fig. 12). Except for CO_2* and large diluent concentrations, the simulations (solid lines) reproduce well measurements (symbols) in Fig. 14 top. The mean relative difference between measurements and simulations reaches 6% for OH* and 4% for CH*. Simulations however largely overesti-

mate the increase of the CO_2* emission intensity. Because dilution has here an opposite effect on the OH* and CO_2* intensities, correction of the OH* chemiluminescence intensity by the CO_2* background intensity now has a larger influence on the results than for experiments conducted at a fixed equivalence ratio $\phi = 0.85$.

When N_2 is used to dilute the flames, the CO_2* intensity remains roughly constant, the CH* emission level slightly increases, and the OH* intensity decreases when the concentration of N_2 increases. However, effects of N_2 dilution remain always weak, with variations limited to $\pm 15\%$ for large diluent concentrations. Simulations better reproduce experiments than for CO_2-diluted flames with a mean relative difference reaching 2%, 5%, and 4% for OH*, CO_2*, and CH*, respectively. The detailed chemistry mechanisms for OH* and CH* and the simplified model for the CO_2* intensity yield overall good results when dilution is made at a fixed adiabatic flame temperature. Independently of the excited radical considered and the diluent nature, the decay of chemiluminescence intensities observed in Fig. 12 when dilution is made at a constant equivalence ratio is attenuated or even canceled-out when the adiabatic flame temperature is kept constant during dilution (see Fig. 14). From that, it is concluded that the temperature reduction induced by dilution at a fixed equivalence ratio is a main contributor to the reduced chemiluminescence intensities observed in Fig. 12. A rough analysis of the reaction paths leading to the formation of excited radicals also points in this direction. For example, Eq. (5) shows that decreasing the temperature decreases the reaction rate of the overall reaction producing CO_2* chemiluminescence. Similarly, the concentration of CO and O generally increases with temperature.

Although the influence of dilution with N_2 or CO_2 on excited radicals emissions is studied here, one must be careful when ap-
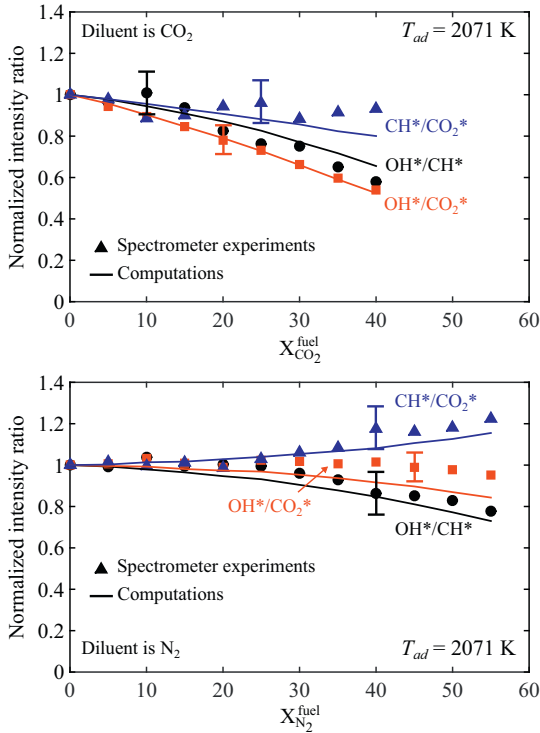
Fig. 15. Measured (symbols) and computed (lines) normalized OH*/CH* (black), OH*/CO$_2$* (red), and CH*/CO$_2$* (blue) intensity ratios as a function of the diluent mole fraction in the fuel when dilution is realized at a fixed adiabatic flame temperature $T_{ad} = 2071$ K. Diluent is CO$_2$ (top) or N$_2$ (bottom). (For interpretation of the references to color in this figure legend, the reader is referred to the web version of this article.)

plying these results to systems such as internal engines with exhaust gas recirculation (EGR). Indeed, the flue gases recirculating in such systems are generally not cooled to a near ambient temperature before injection and are therefore carrying residual enthalpy. After mixing with reactants, the blend temperature is likely to be higher than the temperature with cold diluents, which, as described in the previous paragraph, would most probably benefit excited radicals emissions. In addition, recirculating exhaust gases contain vapor water, whose influence on excited radicals emissions is not studied here.

Taking the sensitivity of chemiluminescence emissions to temperature at face value, additional 1-D FPF simulations that account for heat-losses through thermal radiation are now conducted. A built-in radiation model is used with an optically-thin approximation and thermal radiation from CO$_2$, H$_2$O, CO, and CH$_4$ species is included. For large dilution ratios with CO$_2$, e.g. $X_{CO_2}^{fuel} = 0.35$, the peak temperature is reduced by roughly 3% when the radiation model is activated. In the worst-case scenario, this leads to a reduction of less than 2% of the peak and integrated OH*, CH*, and CO$_2$* chemiluminescence emissions. While non-negligible, the influence of radiation lies within experimental uncertainties. Interpretation of the results presented in this study is therefore independent of whether or not radiation is accounted for.

Figure 15 plots the measured OH*/CH* (black circle), OH*/CO$_2$* (red squares), and CH*/CO$_2$* (blue triangles) intensity ratios as a function of the diluent mole fraction in the fuel for mixtures featuring the same adiabatic flame temperature $T_{ad} = 2071$ K. Results are here again presented for CO$_2$-diluted flames at the top and N$_2$-diluted flames at the bottom and are normalized by the value obtained for the undiluted case. As for dilution at a fixed equivalence ratio $\phi = 0.85$, the three intensity ratios decrease when the

mole fraction of CO$_2$ in the fuel increases. The measured OH*/CO$_2$* intensity ratio drops by more than 40% for $X_{CO_2}^{fuel} = 0.40$. This behavior is also well reproduced by the simulations. This behavior confirms that the OH*/CO$_2$* chemiluminescence intensity ratio is a good indicator to infer the CO$_2$ diluent concentration. Results for the CH*/CO$_2$* and OH*/CH* couples feature a lower SNR with a larger dispersion of the measurements. Simulations only capture the general trend for these couples.

In contrast to dilution experiments conducted at a fixed equivalence ratio, dilution by N$_2$ at a fixed adiabatic flame temperature has a slight influence on the OH*/CH* and CH*/CO$_2$* chemiluminescence intensity ratios. The OH*/CO$_2$* ratio slightly decreases at large N$_2$ dilution concentrations. The OH*/CH* ratio drops by approximately 20% for $X_{N_2}^{fuel} = 0.55$ and the CH*/CO$_2$* ratio increases by more than 20% for the same N$_2$ diluent concentration. These behaviors are relatively well reproduced by the simulations, but the sensitivity of these intensity ratios with respect to dilution remains weak. These indicators cannot be used for sensing N$_2$ dilution.

4. Conclusion

A combined experimental and numerical analysis was carried out to investigate the OH*, CH*, and CO$_2$* chemiluminescence signals in CO$_2$- and N$_2$-diluted CH$_4$/air laminar flames. The main conclusions are:

- For mixtures diluted at a fixed equivalence ratio $\phi = 0.85$, the chemiluminescence intensities from OH* near 307 nm, CH* near 430 nm, and CO$_2$* near 455 nm regularly decrease with increasing the diluent concentration. For N$_2$-diluted flames, the three signals OH*, CH*, and CO$_2$* collapse on the same curve when they are normalized by the signal intensity of the undiluted case. For CO$_2$-diluted flames, the decay rate differs between the OH*, CH*, and CO$_2$* signals. The relative OH* intensity decreases the fastest, then the CH*, and then CO$_2$* signals when the CO$_2$ concentration in the fuel blend is increased.
- The Lindstedt detailed chemistry mechanism [49] extended with sub-mechanisms for the chemistry of OH* and CH* [26] allows to simulate accurately effects of N$_2$ and CO$_2$ dilution on OH* and CH* concentrations. Agreement between experiments and simulations is excellent for OH*, with relative differences smaller than 3% and lying within experimental uncertainties, except for dilution with CO$_2$ at a fixed adiabatic flame temperature where relative differences reach 6%. Differences between simulations and measurements slightly increase for CH* but agreement remains good.
- Because CO$_2$* is mainly produced by a reaction between O and CO species, a model for the CO$_2$* chemiluminescence intensity that does not account for the complex chemistry of CO$_2$* was used in the simulations. Agreement between CO$_2$* chemiluminescence intensity measurements and calculations with this simplified method is overall good. The largest differences are found for large CO$_2$ diluent concentrations when $X_{CO_2}^{fuel} > 0.30$.
- Correction for the CO$_2$* background emission barely alters the measured signal intensity near 307 nm because the contribution of the broadband chemiluminescence from CO$_2$* remains low within the 10 nm bandpass filter centered at 307 nm that is used to examine the OH* emission. Secondly, N$_2$ and CO$_2$ dilutions have similar effects on OH* and CO$_2$* chemiluminescence signals, reducing the detrimental impact of collecting a fraction of light emitted from CO$_2$* when examining the OH* signal around 307 nm.
- The influence of the CO$_2$* background emission needs however to be considered when the CH* emission intensity around 430 nm is investigated. The relatively low CH* signal with re-

spect to the CO_2^* background emission leads to larger imprecisions for estimates of the CH^* intensity.

- The ratio between the OH^* and CO_2^* emission intensities rapidly decreases for CO_2-diluted fuel blends. This combination leads to the largest rate of decrease of the signal as the CO_2 concentration increases. These results indicate that monitoring the OH^*/CO_2^* intensity ratio may be used, with careful initial calibration, to infer the CO_2 concentration in lean CO_2-diluted CH_4/air flames.
- Dilution with N_2 barely changes the OH^*/CO_2^* intensity ratio. This ratio cannot be envisaged to infer the N_2 concentration.
- Results are unchanged if radiative heat losses are taken into account in 1-D FPF simulations.

Acknowledgment

Supplementary material

Supplementary material associated with this article can be found, in the online version, at 10.1016/j.combustflame.2017.01.032.

References

[1] H.N. Najm, P.H. Paul, C.J. Mueller, P.S. Wyckoff, On the adequacy of certain experimental observables as measurements of flame burning rate, Combust. Flame 113 (1998) 312–332.

[2] R. Blonbou, A. Laverdant, S. Zaleski, P. Kuentzmann, Active control of combustion instabilities on a Rijke tube using neural networks, Proc. Combust. Inst. 28 (2000) 747–755.

[3] S. Ducruix, D. Durox, S. Candel, Theoretical and experimental determinations of the transfer function of a laminar premixed flame, Proc. Combust. Inst. 28 (2000) 765–773.

[4] S.-Y. Lee, S. Seo, J. Broda, S. Pal, R. Santoro, An experimental estimation of mean reaction rate and flame structure during combustion instability in a lean premixed gas turbine combustor, Proc. Combust. Inst. 28 (2000) 775–782.

[5] N. Docquier, S. Candel, Combustion control and sensors: a review, Prog. Energy Combust. 28 (2002) 107–150.

[6] Y. Hardalupas, M. Orain, Local measurements of the time-dependent heat release rate and equivalence ratio using chemiluminescent emission from a flame, Combust. Flame 139 (2004) 188–207.

[7] M. Lauer, T. Sattelmayer, On the adequacy of chemiluminescence as a measure for heat release in turbulent flames with mixture gradients, J. Eng. Gas. Turb. Power 132 (2010) 061502 p. 8.

[8] M. Lauer, M. Zellhuber, T. Sattelmayer, C.J. Aul, Determination of the heat release distribution in turbulent flames by a model based correction of OH^* chemiluminescence, J. Eng. Gas. Turb. Power 133 (2011) 1–8.

[9] A. Hossain, Y. Nakamura, A numerical study on the ability to predict the heat release rate using CH^* chemiluminescence in non-sooting counterflow diffusion flames, Combust. Flame 161 (2014) 162–172.

[10] T. Chou, D.J. Patterson, In-cylinder measurement of mixture maldistribution in a l-head engine, Combust. Flame 101 (1995) 45–57.

[11] J. Kojima, Y. Ikeda, T. Nakajima, Spatially resolved measurement of OH^*, CH^*, and C_2^* chemiluminescence in the reaction zone of laminar methane/air premixed flames, Proc. Combust. Inst. 28 (2000) 1757–1764.

[12] N. Docquier, S. Belhalfaoui, F. Lacas, N. Darabiha, C. Rolon, Experimental and numerical study of chemiluminescence in methane/air high-pressure flames for active control applications, Proc. Combust. Inst. 28 (2000) 1765–1774.

[13] B. Higgins, M. McQuay, F. Lacas, J. Rolon, N. Darabiha, S. Candel, Systematic measurements of OH chemiluminescence for fuel-lean, high-pressure, premixed, laminar flames, Fuel 80 (2001) 67–74.

[14] N. Docquier, F. Lacas, S. Candel, Closed-loop equivalence ratio control of premixed combustors using spectrally resolved chemiluminescence measurements, Proc. Combust. Inst. 29 (2002) 139–145.

[15] T. Muruganandam, B.-H. Kim, M. Morrell, V. Nori, M. Patel, B. Romig, J. Seitzman, Optical equivalence ratio sensors for gas turbine combustors, Proc. Combust. Inst. 30 (2005) 1601–1609.

[16] C. Panoutsos, Y. Hardalupas, A. Taylor, Numerical evaluation of equivalence ratio measurement using OH^* and CH^* chemiluminescence in premixed and non-premixed methane–air flames, Combust. Flame 156 (2009) 273–291.

[17] J. Ballester, T. García-Armingol, Diagnostic techniques for the monitoring and control of practical flames, Prog. Energy Combust. 36 (2010) 375–411.

[18] T. García-Armingol, J. Ballester, A. Smolarz, Chemiluminescence-based sensing of flame stoichiometry: influence of the measurement method, Measurement 46 (2013) 3084–3097.

[19] T. García-Armingol, J. Ballester, Influence of fuel composition on chemiluminescence emission in premixed flames of $CH_4/CO_2/H_2/CO$ blends, Int. J. Hydrogen. Energy 39 (2014) 20255–20265.

[20] T. García-Armingol, Y. Hardalupas, A. Taylor, J. Ballester, Effect of local flame properties on chemiluminescence-based stoichiometry measurement, Exp. Therm. Fluid. Sci. 53 (2014) 93–103.

[21] J.-M. Samaniego, F.N. Egolfopoulos, C.T. Bowman, CO_2^* chemiluminescence in premixed flames, Combust. Sci. Technol. 109 (1995) 183–203.

[22] M. Kopp, M. Brower, O. Mathieu, E. Petersen, F. Güthe, CO_2^* chemiluminescence study at low and elevated pressures, Appl. Phys. B 107 (2012) 529–538.

[23] R. Porter, A. Clark, W. Kaskan, W. Browne, A study of hydrocarbon flames, Symp. (Int.) Combust. 11 (1967) 907–917.

[24] K. Walsh, M. Long, M. Tanoff, M. Smooke, Experimental and computational study of CH, CH^*, and OH^* in an axisymmetric laminar diffusion flame, Symp. (Int.) Combust. 27 (1998) 615–623.

[25] M. Tamura, P.A. Berg, J.E. Harrington, J. Luque, J.B. Jeffries, G.P. Smith, D.R. Crosley, Collisional quenching of CH(A), OH(A), and NO(A) in low pressure hydrocarbon flames, Combust. Flame 114 (1998) 502–514.

[26] J. Luque, J. Jeffries, G. Smith, D. Crosley, K. Walsh, M. Long, M. Smooke, CH(A-X) and OH(A-X) optical emission in an axisymmetric laminar diffusion flame, Combust. Flame 122 (2000) 172–175.

[27] G.P. Smith, J. Luque, C. Park, J.B. Jeffries, D.R. Crosley, Low pressure flame determinations of rate constants for OH(A) and CH(A) chemiluminescence, Combust. Flame 131 (2002) 59–69.

[28] S.A. Carl, M.V. Poppel, J. Peeters, Identification of the $CH + O_2$ OH(A) + CO reaction as the source of OH(AX) chemiluminescence in $C_2H_2/O/H/O_2$ atomic flames and determination of its absolute rate constant over the range $T = 296$ to 511 K, J. Phys. Chem. A 107 (2003) 11001–11007.

[29] K. Becker, H. Brenig, T. Tatarczyk, Lifetime measurements on electronically excited $CH(A2\Delta)$ radicals, Chem. Phys. Lett. 71 (1980) 242–245.

[30] K. Devriendt, H.V. Look, B. Ceursters, J. Peeters, Kinetics of formation of chemiluminescent $CH(A2\Delta)$ by the elementary reactions of $C_2H(X2\Sigma+)$ with O(3P) and $O_2(X3\Sigma g)$: A pulse laser photolysis study, Chem. Phys. Lett. 261 (1996) 450–456.

[31] R.M.I. Elsamra, S. Vranckx, S.A. Carl, $CH(A2\Delta)$ formation in hydrocarbon combustion: the temperature dependence of the rate constant of the reaction $C_2H + O_2$ $CH(A2\Delta) + CO_2$, J. Phys. Chem. A 109 (2005) 10287–10293. PMID: 16833323.

[32] D.L. Baulch, D.D. Drysdale, J. Duxbury, S.J. Grant, Evaluated kinetic data for high temperature reactions, Butterworths, London, 1976.

[33] J. Kojima, Y. Ikeda, T. Nakajima, Basic aspects of OH(A), CH(A), and $C_2(d)$ chemiluminescence in the reaction zone of laminar methane–air premixed flames, Combust. Flame 140 (2005) 34–45.

[34] J. Kojima, Y. Ikeda, T. Nakajima, Multi-point time-series observation of optical emissions for flame-front motion analysis, Meas. Sci. Technol. 14 (2003) 1714–1724.

[35] V.N. Nori, J.M. Seitzman, CH^* chemiluminescence modeling for combustion diagnostics, Proc. Combust. Inst. 32 (2009) 895–903.

[36] P. Weiland, Biogas production: current state and perspectives, Appl. Microbiol. Biotechnol. 85 (2010) 849–860.

[37] S. Rasi, A. Veijanen, J. Rintala, Trace compounds of biogas from different biogas production plants, Energy 32 (2007) 1375–1380.

[38] J.D. Murphy, E. McKeogh, G. Kiely, Technical/economic/environmental analysis of biogas utilisation, Appl. Energy 77 (2004) 407–427.

[39] J.B. Holm-Nielsen, T.A. Seadi, P. Oleskowicz-Popiel, The future of anaerobic digestion and biogas utilization, Bioresource Technol. 100 (2009) 5478–5484.

[40] I. Gokalp, E. Lebas, Alternative fuels for industrial gas turbines (aftur), Appl. Therm. Eng. 24 (2004) 1655–1663.

[41] Y. Lafay, B. Taupin, G. Martins, G. Cabot, B. Renou, A. Boukhalfa, Experimental study of biogas combustion using a gas turbine configuration, Exp. Fluids 43 (2007) 395–410.

[42] B.B. Sahoo, N. Sahoo, U.K. Saha, Effect of engine parameters and type of gaseous fuel on the performance of dual-fuel gas diesel engines—a critical review, Renew. Sust. Energy Rev. 13 (2009) 1151–1184.

[43] K.K. Gupta, A. Rehman, R.M. Sarviya, Bio-fuels for the gas turbine: a review, Renew. Sust. Energy Rev. 14 (2010) 2946–2955.

[44] I.D. Bedoya, S. Saxena, F.J. Cadavid, R.W. Dibble, M. Wissink, Experimental study of biogas combustion in an HCCI engine for power generation with high indicated efficiency and ultra-low nox emissions, Energ. Convers. Manag. 53 (2012) 154–162.

[45] S.E. Hosseini, M.A. Wahid, Development of biogas combustion in combined heat and power generation, Renew. Sust. Energy Rev. 40 (2014) 868–875.

[46] G.P. Smith, D.M. Golden, M. Frenklach, N.W. Moriarty, B. Eitneer, M. Goldenberg, C.T. Bowman, R.K. Hanson, S. Song, J.W.C. Gardiner, V.V. Lissianski, Z. Qin, available at http://www.me.berkeley.edu/gri-mech/(1999).

[47] A. Mazas, B. Fiorina, D. Lacoste, T. Schuller, Effects of water vapor addition on the laminar burning velocity of oxygen-enriched methane flames, Combust. Flame 158 (2011) 2428–2440.

[48] S. Candel, T. Schmitt, N. Darabiha, Progress in transcritical combustion : experimentation, modeling and simulation, Proceedings of 23rd ICDERS, Irvine USA (2011).

[49] P. Lindstedt, Modeling of the chemical complexities of flames, Symp. (Int.) Combust. 27 (1998) 269–285.

[50] V. Nori, Modeling and analysis of chemiluminescence sensing for syngas, methane and Jet-A combustion, Georgia Institute of Technology, 2008 Ph.D. thesis.

[51] P. Glarborg, L.L.B. Bentzen, Chemical effects of a high CO_2 concentration in oxy-fuel combustion of methane, Energy Fuels 22 (2008) 291–296.

[52] F. Halter, F. Foucher, L. Landry, C. Mounaïm-Rousselle, Effect of dilution by nitrogen and/or carbon dioxide on methane and iso-octane air flames, Combust. Sci. Technol. 181 (2009) 813–827.

[53] X. Hu, Q. Yu, J. Liu, N. Sun, Investigation of laminar flame speeds of $CH_4/O_2/CO_2$ mixtures at ordinary pressure and kinetic simulation, Energy 70 (2014) 626–634.

[54] C. Law, D. Zhu, G. Yu, Propagation and extinction of stretched premixed flames, Symp. (Int.) Combust. 21 (1988) 1419–1426.

[55] B.M. Cetegen, T.A. Ahmed, Experiments on the periodic instability of buoyant plumes and pool fires, Combust. Flame 93 (1993) 157–184.

[56] T. Yuan, D. Durox, E. Villermaux, An analogue study for flame flickering, Exp. Fluids 17 (1994) 337–349.

[57] D. Durox, S. Ducruix, Concerning the location of schlieren limit in premixed flames, Combust. Flame 120 (2000) 595–598.

[58] G.S. Settles, Schlieren and shadowgraph techniques, Springer-Verlag Berlin Heidelberg, 2001.

[59] H. Guo, J. Min, C. Galizzi, D. Escudié, F. Baillot, A numerical study on the effects of $CO_2/N_2/Ar$ addition to air on liftoff of a laminar CH_4/Air diffusion flame, Combust. Sci. Technol. 182 (2010) 1549–1563.